IOP Publishing | International Atomic Energy Agency Nuclear Fusion

Nucl. Fusion **62** (2022) 086008 (12pp) https://doi.org/10.1088/1741-4326/ac6682

Divertorlets concept for low-recycling fusion reactor divertor: experimental, analytical and numerical verification

F. Saenz[1], Z. Sun[2], A.E. Fisher[1], B. Wynne[1] and E. Kolemen[1,2,*]

[1] Princeton University, Princeton, 08540, United States of America
[2] Princeton Plasma Physics Laboratory, Princeton, 08540, United States of America

E-mail: ekolemen@pppl.gov

Received 8 December 2021, revised 5 April 2022
Accepted for publication 12 April 2022
Published 1 June 2022

Abstract

The 'divertorlets' concept is a potential non-evaporative liquid metal solution for heat removal at low recycling regime. A toroidal divertorlets prototype was built and tested in LMX-U at Princeton Plasma Physics Laboratory to evaluate the performance of this configuration. In this paper, details of the design, experimental results, comparison with analytical theory and MHD numerical simulations of toroidal divertorlets are covered. Experiments, analytical model and simulations showed agreement and allowed the projection of operation properties at higher magnetic flux densities (reactor-like operation), proving the concept to be a compelling solution for divertor applications.

Keywords: liquid metals, plasma facing components, MHD simulations

(Some figures may appear in colour only in the online journal)

1. Introduction

Plasma facing components (PFCs) of fusion reactors can experience extreme heat flux in the divertor region. Particularly, divertors have reached over 10 MW m^{-2} in experimental devices and may increase in commercial reactors [2]. Solid PFCs for divertor solutions are limited in handling this heat flux and experience irreversible damage, requiring frequent shutdowns for maintenance.

Liquid metals have been proposed to address these challenges as they can carry away heat and self-heal through replenishment. In particular, lithium is the primary candidate for its chemical affinity with hydrogen isotopes, allowing low hydrogen recycling conditions [3–6]. The improvements in energy confinement and plasma performance due to low-recycling conditions have been widely demonstrated [7]: reduced impurity radiation [8], higher edge temperatures, reduction of ELMs and smaller energy losses through temperature gradient-driven instabilities [3, 9–11].

Besides the analysis of the most favorable operating liquid metal, several concepts of liquid-metal-plasma-facing components (LM-PFCs) have been proposed as solutions for a divertor and no consensus has been reached about the most advantageous configuration [4–6]. Among weaknesses outlined [1, 4–6], flow speed of the liquid metal is one of the most important as it contributes to MHD drag. Fast-flowing concepts encounter severe MHD drag for the system with risk of piling and splashing [12]. On the other hand, slow-flowing LM-PFCs use liquid metal flows as an intermediate heat removal mechanism, achieving reduced MHD drag but may not avoid evaporation [1].

The divertorlets concept is an alternative that combines the advantages of both operating regimes: minimized MHD drag due to relatively small velocities while addressing issues such as evaporation, operation power, and liquid metal inventory. Moreover, reduced exposure time of the liquid metal to the plasma (a quality inherent to fast-flowing concepts) is also achieved by the divertorlets concept through the minimization of the flow path length [1]. The latter condition leads to lower temperatures of the operating liquid metal and reduced evaporation [12].

* Author to whom any correspondence should be addressed.

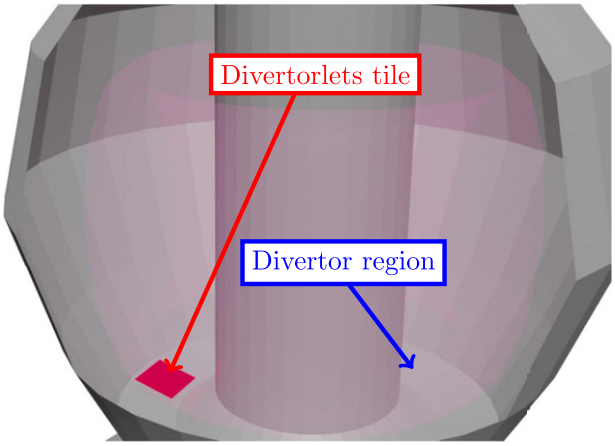

Figure 1. Position of a divertorlets tile in a fusion device. Reprinted from Nuclear Materials and Energy, Vol 25/100855, A.E. Fisher, Z. Sun, E. Kolemen, Liquid metal 'divertorlets' concept for fusion reactors, pages 1–11, Reprinted from [1], Copyright (2020), with permission from Elsevier. CC BY-NC-ND 4.0.

Furthermore, the divertorlets concept offers a constant replacement of the liquid metal surface that faces the plasma. For the case of liquid lithium, the latter works in favor of the hydrogenic uptake by avoiding the presence of saturated-liquid-metal-facing surfaces. Thus, the low-recycling regime would be possible and compatible with a continuous operation scenario [7, 12].

In this article, the configuration tested was the toroidal divertorlets [1]. First, geometry and operation of the system are described. Next, details about experimental measurements and simulations performed are listed. A comparison between results from experiments and simulations at $|\mathbf{j}_e \times \mathbf{B}_0| \leqslant 0.23$ MN m^{-3} is shown. This comparison serves as a benchmark for optimizations of the divertorlets configuration at higher magnetic field intensities. Finally, optimization directions for divertorlets are explained and projections of power requirements and permissible heat flux for operation at the reactor scale are included.

1.1. The toroidal divertorlets concept

A divertorlets system is intended to be placed in the divertor region of a tokamak reactor (see figure 1). The toroidal divertorlets consists of direction-alternating flow paths that are connected by a layer of liquid metal at either end. The flow paths are separated by 'slats' that are oriented toroidally (see figure 2(*a*)). These slats generate channels for each of the flow paths.

A similar geometry to that of a divertorlets system is the LiMIT concept [13], but these two concepts operate differently. While the LiMIT concept uses a thermally induced electric current to generate fluid motion, a divertorlets configuration requires a unidirectional external current that generates a current distribution $\mathbf{j}_e$ that is modified by strategically placed conductors (see figure 2(*b*)).

Corresponding to a previous liquid metal divertor concept called 'actively convected liquid metal divertor' [14], the motion of the liquid metal in a divertorlets configuration is generated with the externally applied current in combination with an external (toroidal) magnetic field $\mathbf{B}_0$. Thus, $\mathbf{j}_e \times \mathbf{B}_0$ drives the body force, and the difference of $\mathbf{j}_e$ between consecutive channels drives the flow due to the designed slat geometry.

The operational efficiency of the toroidal divertorlets intrinsically depends on the necessary liquid metal inventory, cooling requirements, free surface conditions and the $\mathbf{j}_e \times \mathbf{B}_0$ force distribution generated. Calculations and scaling for a reactor scenario were presented in [1] using a set of parameters for an ITER-like device.

The final design of the toroidal divertorlets would require tests in reactor-like conditions. However, the prototype tested for this paper had dimensions that could ease the manufacturing process and measurements of flow speeds on the device. Tests were performed at different magnitudes for the background magnetic field $\mathbf{B}_0$ and externally applied currents I_0. Moreover, simulation results of toroidal divertorlets were compared and validated with experimental results. Finally, projections on the performance of toroidal divertorlets were calculated based on an analytical model derived on results from simulations.

2. Methodology

For the toroidal divertorlets device tested, the operating liquid metal was an alloy with 67% Ga, 20.5% In and 12.5% Sn, commonly referred to as galinstan. A polycarbonate box was used as a container for liquid metal and the slats. A slat consisted of a copper–G10–copper sandwich. The purpose of the G10 sheet was to force the electric current to pass through the conductors and not through the slats (see figure 3). For reactor scenarios, the G10 insulator would work as thermal insulation between the flow passing through different channels. All experiments were performed at room temperature.

Copper was also used for the conductors between the slats, to ease the manufacturing process and for its relatively high electrical conductivity compared to the conductivity of galinstan. Dimensions for all components of the toroidal divertorlets were chosen based on dimensional constraints from the LMX-U test stand and simulation results. Figure 4 shows a general diagram of dimensions and table 1 shows the dimensions used for experimental results.

Finally, table 2 shows the properties of the galinstan alloy used for experiments. These properties were also used for other calculations/simulations. In addition, properties of liquid lithium are also included for calculations shown in section 3.4.

2.1. Experiments

All experiments were performed using the LMX-U facility at PPPL. An electromagnet was used to generate background magnetic fields up to 0.33 T. Spatial variation of the magnetic field intensity is less than 5% for the test stand used [18]. Five different magnetic field intensities were used for measurements, specifically 0.1 T, 0.2 T, 0.27 T, 0.3 T and 0.33 T.

External electric current was applied using four electrodes connected to copper plates on each side of the divertorlets. The

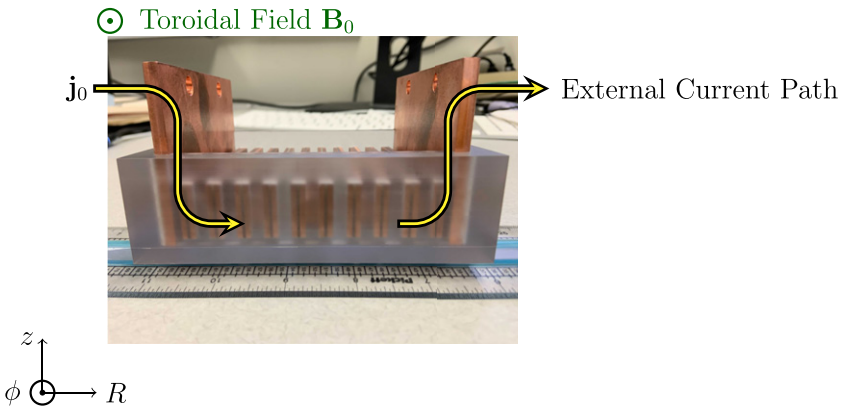

(a) Side view of toroidal divertorlets.

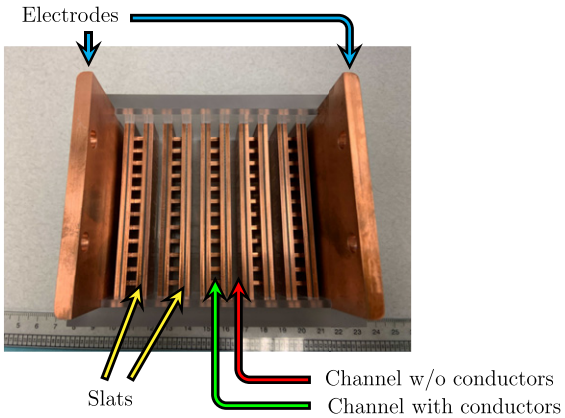

(b) Top view of toroidal divertorlets.

Figure 2. Toroidal divertorlets tile used for experiments.

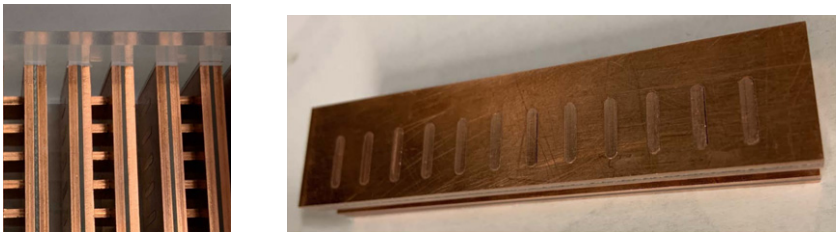

Figure 3. Close view of slats (Copper - G10 - Copper Sandwich).

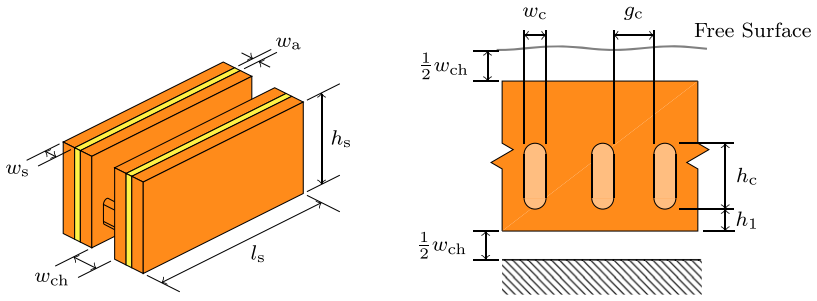

(a) Side view of toroidal divertorlets.

(b) Cutting plane view at center of channel with upward flow.

Figure 4. Diagram with dimensions of toroidal divertorlets.

Table 1. Dimensions of divertorlets for experimental results.

Parameter	(mm)
Slat width w_s	2.0
Slat height h_s	20.3
G10-sheet thickness w_a	0.8
Channel width w_{ch}	5.1
Slat height h_s	20.3
Slat length l_s	82.3
Conductor width w_c	3.0
Gap between conductors g_c	3.89
Conductor height h_c	7.5
h_1	4

Table 2. Properties of galinstan alloy and liquid lithium.

Property	GaInSn at room temperature [15, 16]	Li at 310 °C [17]
Density ρ (kg m^{-3})	6360	516
Therm. conductivity k W (m^{-1} K^{-1})	296	4300
Electrical conductivity σ (MS m^{-1})	3.1	3.341
Viscosity μ (Pa s)	0.0019	3.0
Heat capacity c_p (J (kg^{-1} K^{-1}))	366.5	4169

Figure 5. Plastic tubes used for velocity measurements.

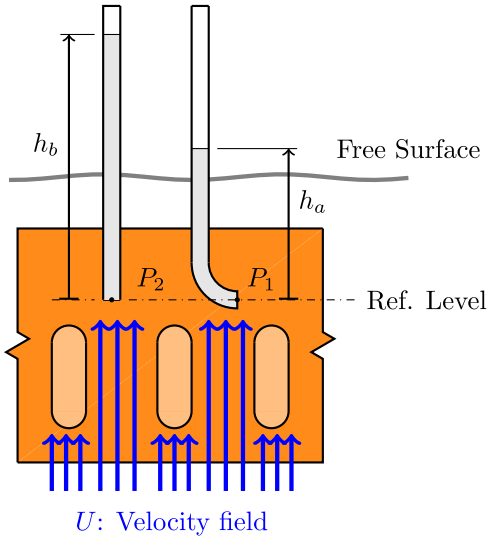

Figure 6. Cutting plane view at the center of channel with upward flow and installed tubes (channel with conductors). Note: drawing not to scale.

current source used generated currents up to 900 A. Measurements were performed using values of current from 100 A to 900 A, with 100 A increments.

Velocity measurements were performed using a straight tube and an L-shaped tube (see figure 5), which follow the same mechanism of a pitot tube. Both plastic tubes were placed in a channel of the divertorlets prototype with upward flow velocity (see figure 6).

In the aforementioned channel, the lower end of the straight tube was located at the same height as the center of the the cross section of the lower end of the L-shaped tube. The L-shaped tube measured the static pressure generated by the velocity field, and the straight tube measured an estimate of the sum of dynamic and static pressures. These pressures generated columns of galinstan in each tube with different heights (see figure 6).

The upper ends of both tubes were open to atmosphere during experiments, then $P_2 = P_{atm} + \rho g h_b$ and $P_1 = P_{atm} + \rho g h_a$, where ρ is the mass density of galinstan, g is the standard gravity, and P_{atm} is the atmospheric pressure. If the effect of the tubes on the velocitiy field is ignored, then $P_1 + \frac{1}{2}\rho|\mathbf{U}|^2 \approx P_2$.

Hence, the upward flow speed can be expressed as follows:

$$|\mathbf{U}| \approx \sqrt{2g\Delta h}; \quad \Delta h = h_b - h_a. \tag{1}$$

Equation (1) was used to approximate flow velocities from the measurements of height differences Δh at different externally applied currents I_0 and magnetic field strengths $\mathbf{B}_0$. As a note, galinstan oxidizes almost immediately after having contact with oxygen. All the experiments were performed at open atmosphere and it was not possible to avoid/reduce oxidation. Galinstan oxides accumulated at the free surface were removed and galinstan was constantly replenished during experiments.

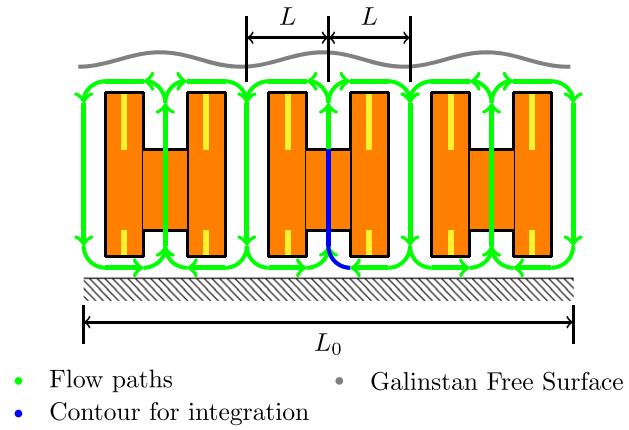

Figure 7. Velocity contour from side view of toroidal divertorlets. Note: figure not to scale.

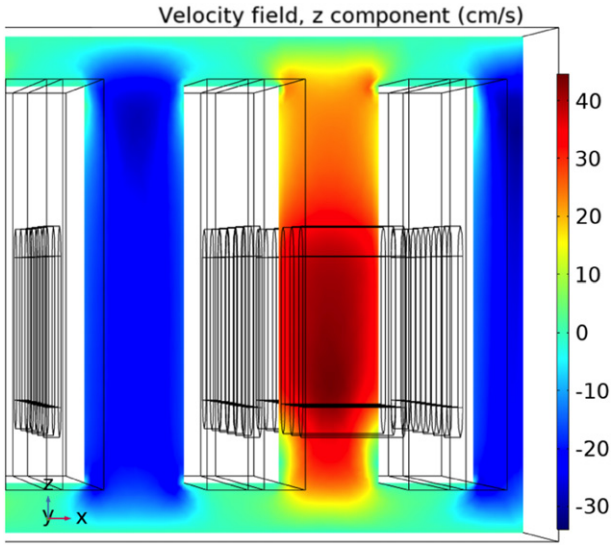

Figure 8. Simulation result at 0.33 T, 900 A: vertical component of flow velocity field.

2.2. Simulation

The purpose of simulations was to compare the magnitudes of flow velocities from simulations and experimental results. The tubes used for experiments (see figure 6) measured an average velocity, but simulation results yield a full velocity field. In order to be able to compare these, the contour shown in figure 7 was used to estimate the average-upward-flow velocities from simulations.

Simulations were done with COMSOL 5.6 using the CFD and AC/DC modules [19–21]. The setup for the simulation consisted of a non-deforming liquid metal box. The domain for the liquid metal employed no-slip boundary conditions on all physical surfaces, except on the top surface, where a slip boundary condition was applied. Externally applied electric currents were created by specifying a constant and uniform current density at a terminal, and selecting the opposite boundary for the electrical ground. Other external boundaries of the liquid metal box were treated as electrically insulated.

The slats were placed inside the liquid metal box, and boundary conditions for these components satisfied continuity for the electric current density and electric potential. All appropriate material properties were applied to components within the domain. The electrical conductivity of copper used for simulations was 59.97 MS m^{-1} [22]. The velocity field was caused by the balance between the $\mathbf{j} \times \mathbf{B}$ forces (pumping from the external current and MHD drag) and viscous forces from the fluid.

3. Results and discussion

3.1. Experiments

Experimental results are shown in figure 9. Flow speeds were calculated using equation (1). It can be observed that there is an increasing flow speed with increasing external current I_0. This result was expected given that the pumping force from the external current is linearly proportional to the difference of current densities between consecutive channels. Moreover, there is also an increasing flow speed with increasing magnetic field strength at all values of external current I_0. These two observations will be the the focus of the comparison with simulation results.

Finally, it must be noted that the direction-alternating channel flow of the divertorlets concept generates a deformed free surface during operation (wavy pattern, see figure 5, 4 mm was the maximum peak-to-valley height observed during experiments, at 900 A, 0.3 T). This could cause intense evaporation of the liquid metal depending on the angle of incidence of the heat flux. The latter could be solved by having a divertorlets surface contour along a closed flux surface.

However, it must be recalled that the dimensions chosen for the prototype tested were such to allow velocity measurements, particularly the distance L (see figure 7). The parameter L is expected to be smaller for reactor operation to achieve the minimization of the exposure time of the liquid metal to the plasma (see section 3.5). The reduction of the distance L will allow the attainment of free surfaces with more uniform shapes and the avoidance of critical heat flux conditions due to ripples.

3.2. Simulation

Simulation results are shown in figure 9. Additionally, figure 8 displays a general plot of the direction-alternating flow paths of a divertorlets system. A first observation is the increasing upward flow speed u_{avg} with increasing externally applied I_0, which matches the experimental results obtained. However, there is a change in the flow speed trend with respect to magnetic field strengths at $I_0 = 500$ A and above. From experiments, there is an increasing flow speed with increasing magnetic field strength, but from simulations, there is a peak flow speed at 0.2 T and decreasing flow speed with $|\mathbf{B}_0| > 0.2$ T.

The latter difference between trends with respect to magnetic field strength can be explained by considering pressure drops that the plastic tubes used for measurements impose on the system and liquid metal oxidation during experiments.

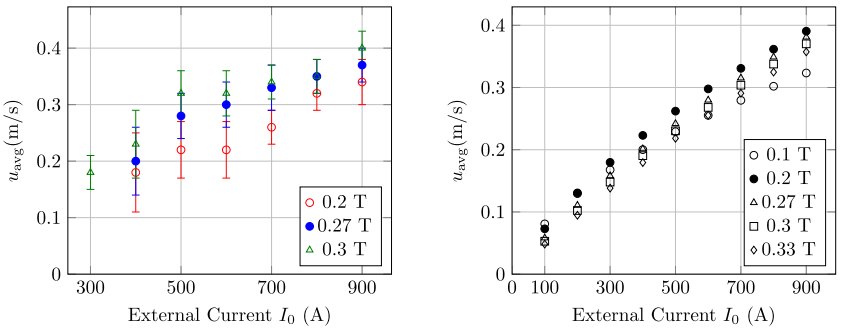

(a) Experimental results (b) Simulation results

Figure 9. Results from experiments and simulations for a Cu–GaInSn divertorlets prototype.

The pressure drop caused by the plastic tubes was evaluated with results from simulations that included tubes with the shapes of those used during experiments. The setup for these simulations is shown in figure 10(*a*). Simulations were performed with $I_0 = 900$ A at different values of magnetic flux density (0.1 T, 0.2 T, 0.27 T, 0.3 T and 0.33 T). The pressure difference $\Delta P = P_2 - P_1$ is estimated directly from simulation results, and the expected velocity measurements $|\mathbf{U}| = \sqrt{\frac{2\Delta P}{\rho}}$ are shown in figure 10(*b*).

From figure 10, it is observable that the tubes generate a significant pressure drop that changes the flow-speed trend shown in figure 9. For 0.2 T $< |\mathbf{B}_0| <$ 0.33 T, the combination of a pressure drop from the plastic tubes and MHD-drag variations due to liquid-metal oxidation/copper corrosion changed the magnetic flux density at which the peak flow speed occurs.

Liquid metal oxidation would reduce the electrical conductivity of the galinstan alloy during experiments, and consequently decrease MHD drag in the system. Moreover, the attachment of a layer of galinstan oxides at the walls of the slats was observed after pouring out the galinstan from the divertorlets box.

In addition, corrosion of the faces of the copper slats occurs after being exposed to galinstan [23]. This layer of oxides and corroded surfaces reduce the effective conductivity of the boundaries that the galinstan flow has contact with, reducing the MHD drag in the system.

A reduction of MHD drag in a divertorlets system would cause the peak flow speed to happen at magnetic field strengths higher than 0.2 T, given that MHD is proportional to $|\mathbf{B}|^2$. Measurements to quantify the effect of a galinstan oxide layer at the walls were not performed and this fact is just left as a source of error for experimental measurements.

Finally, it must be noted that the simplified setup used for simulations assumed a fixed shape for the liquid metal, when in reality it is a deformable domain, particularly at the top free surface. The inaccuracies implied by this simplification are minimized if the deformations at the free surface are relatively small in such a way that the resulting shape is similar to that of the rectangular prism used for simulations. The magnitude of these deformations is proportional to the flow speed of the divertorlets system. Based on experimental and simulation results, the agreement is observable up to flow speeds $\sim$0.4 m s^{-1} (see figure 9).

3.3. Analytical model

Once the simulation file was validated with experiments, an analytical model to calculate flow speeds on the toroidal divertorlets was derived. Consider a steady-state pressure balance along a liquid-metal flow path around a slat (see figure 7 for a simplified diagram of flow paths):

$$\Delta P_{j\times B} - \Delta P_{\text{visc}} \approx 0. \tag{2}$$

In equation (2), ΔP_{visc} is the pressure drop due to viscous losses and $P_{j\times B}$ represents the pressure difference caused by the total electric current through the liquid metal. The total current density is expressed in equation (3). Additionally, the direction of the main components of the current densities around a flow path is shown in figure 11. An expansion of the $\Delta P_{j\times B}$ term is in equation (4).

$$\mathbf{j} = \mathbf{j}_e + \sigma(\mathbf{E} + \mathbf{U}\times\mathbf{B}). \tag{3}$$

Furthermore, in equation (3), $\mathbf{j}_e$ is current density produced by the externally applied current I_0. A portion of the total current in the channels with conductors is carried through these components, producing a current density difference in the liquid metal in consecutive channels. In equation (4), $(\Delta\mathbf{j}_e)_{\text{avg}}$ takes into account this effect and it represents the difference of average current densities between consecutive channels.

$$\Delta P_{j\times B} \approx (\Delta\mathbf{j}_e)_{\text{avg}}|\mathbf{B}|(h_s + w_{ch}) + \sigma\oint_{\text{Flow Path}}(\mathbf{E}+\mathbf{U}\times\mathbf{B})\times\mathbf{B}\cdot\mathrm{d}l. \tag{4}$$

$(\Delta\mathbf{j}_e)_{\text{avg}}$ can be expressed as $(\Delta\mathbf{j}_e)_{\text{avg}} \approx \eta_j I_0$ [1]. η_j is a coefficient that takes into account the arrangement, dimensions and electrical properties of the components of the slats. For the case of the Cu–GaInSn divertorlets prototype tested for this paper, $\eta_j \approx 374.98$ m^{-2} (calculated from simulation results).

Since $\mathbf{E}$ satisfies $\nabla\cdot\mathbf{E} = -\nabla\cdot(\mathbf{U}\times\mathbf{B})$, its magnitude can be approximated as $|\mathbf{E}| \approx C_E|\mathbf{U}\times\mathbf{B}|$. The C_E coefficient can be calculated from simulation results as $\frac{|\mathbf{E}|_{\text{avg}}}{|\mathbf{U}\times\mathbf{B}|_{\text{avg}}}$. The component of $\mathbf{E}$ used for the calculation of $|\mathbf{E}|_{\text{avg}}$ is the component

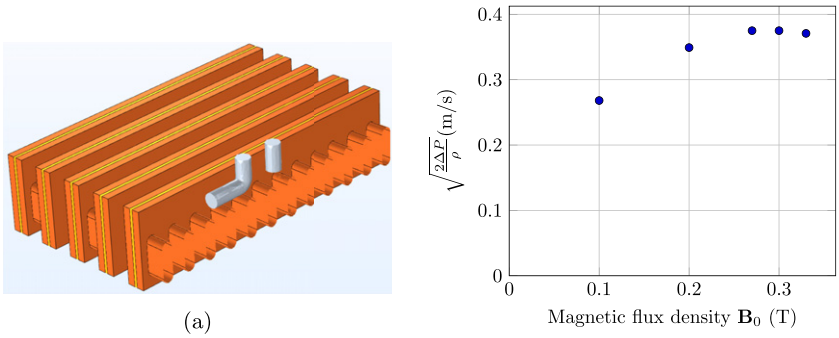

(a) (b)

Figure 10. Setup and results from simulations with plastic tubes.

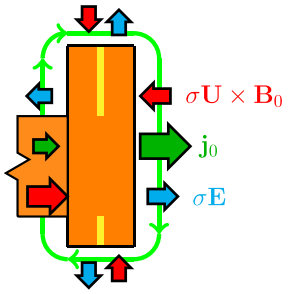

(a) Main components of electric current densities around a flow path.

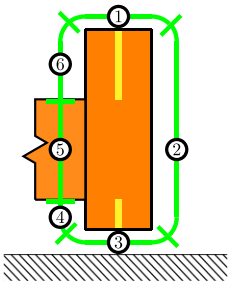

(b) Sections Δs_i of a split flow path around a slat.

Figure 11. Simplified diagram of a slat of a divertorlets prototype.

that is perpendicular to the flow path and the external magnetic field $\mathbf{B_0}$. The same procedure was applied to calculate $|\mathbf{U} \times \mathbf{B}|_{\text{avg}}$. The average values of these vector components were calculated on the cross-sectional area of the liquid metal perpendicular to the flow path highlighted in figure 11.

It must be noted that the coefficient C_E is intrinsic to the specific geometry being tested and its applicability for other geometries/dimensions must be reviewed. Figure 12 shows a plot for the C_E coefficient along the channel with conductors (flow path is highlighted in green). Particularly, along this path, the C_E coefficient is significantly reduced ($C_E \leqslant 0.6$).

Moreover, C_E is relatively constant along the path highlighted in blue in figure 12 ($C_E \sim 0.9$). The difference of magnitude of C_E between the green and blue paths is because of the recycling of the induced current $\sigma(\mathbf{E} + \mathbf{U} \times \mathbf{B})$ in the liquid metal [24]. The presence of electrical conductors along the green path allows the recycling of the electric current to occur through these components, not through the liquid metal strictly. The pumping effect due to current recycling is lost due to the presence of these components, which results in increased MHD drag in the channels with conductors.

Based on figure 12, the expression for the pumping force from $\mathbf{E}$ is simplified in equation (5) by splitting the flow path in 6 sections (see figure 11(*b*)). Each section has a length Δs_i ($i = 1, 2, \ldots, 6$) and the magnitude of $\mathbf{E}$ is approximated with the average $C_{E,i}$ in those sections. It was assumed that the C_E ratio does not change at different magnetic fields $\mathbf{B}_0$ and currents I_0, and verified later with simulation results (see figure 15).

Moreover, in equation (5), C_U is a coefficient that takes into account the flow speed variation due to the change of cross-section area along a flow path. In general, $C_{U,i} = 1$ along all sections Δs_i of a flow path, except for Δs_5, where $C_{U,5} = \frac{A_0}{A_c}$. Moreover, A_0 and A_c are the cross-sectional areas of the channels with downward and upward flow, respectively. Hence, the expression for MHD drag is simplified in equation (5). The result in equation (5) is similar to the expression obtained by [25] to approximate the MHD-drag pressure drop in pipe flows.

$$\begin{aligned}\left|\oint_C (\mathbf{E} + \mathbf{U} \times \mathbf{B}) \times \mathbf{B} \cdot \mathrm{d}l\right| &\approx |\mathbf{U}||\mathbf{B}_0|^2 \oint_{\text{Flow Path}} (1 - C_E) C_U \mathrm{d}l \\ &\approx |\mathbf{U}||\mathbf{B}_0|^2 \sum_{n=1}^{6} C_{M,i} C_{U,i} \Delta s_i; \quad C_M = 1 - C_E. \end{aligned} \tag{5}$$

ΔP_{visc} represents the pressure drop produced by viscous losses on a flow path. Drag losses can be approximated as $\frac{1}{2}\rho C_{\text{D}}|\mathbf{U}|^2$, where ρ is the mass density of galinstan and C_{D} is the drag coefficient. C_{D} depends on the geometry of the obstacles/bifurcations/bends encountered by the liquid following the flow path.

For the case of divertorlets, pressure drops were considered due to the presence of conductors ($(C_{\text{D}})_{\text{conds}}$) in some channels and the branch flow ($(C_{\text{D}})_{\text{branch}}$) at the corners of the slats. The coefficients were $(C_{\text{D}})_{\text{conds}} = 0.8$ [26] and $(C_{\text{D}})_{\text{branch}} = 1.5$ [27]. The total expression for viscous losses can be expressed as follows:

$$\Delta P_{\text{visc}} \approx \frac{1}{2}\rho|\mathbf{U}|^2 \left[\left(\frac{A_0}{A_c}\right)^2 (C_{\text{D}})_{\text{conds}} + 2(C_{\text{D}})_{\text{branch}}\right]. \tag{6}$$

Finally, the magnetic Reynolds number $R_{\text{m}} \ll 1$, then $\mathbf{B} \approx \mathbf{B}_0$. After applying all these simplifications to equation (2), an estimate of the average upward flow velocity for divertorlets was calculated at different currents I_0 and magnetic field strengths $\mathbf{B}_0$. Results from this analytical model are shown

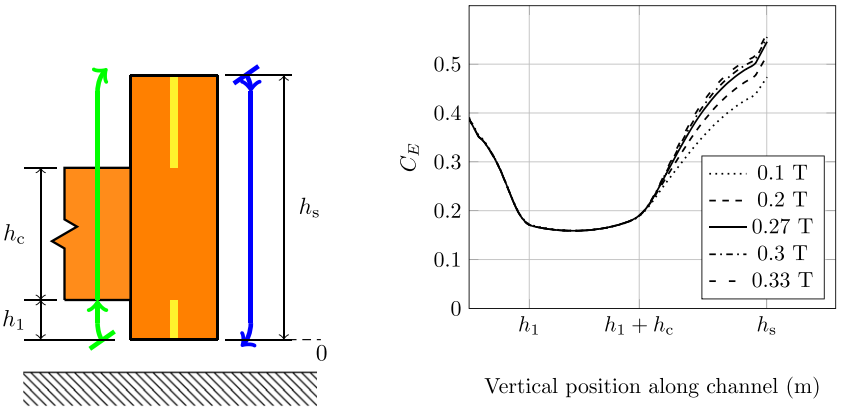

Figure 12. Ratio C_E along channel with conductors for Cu–GaInSn divertorlets. Plot on the right shows the values of C_E of the section highlighted in green. Results shown from simulations with $I_0 = 900$ A.

in section 3.4. The agreement found between the analytical model and simulation results validated the applicability of this analytical model for projections at higher magnetic field strengths.

3.4. MHD-drag reduction

Following the results presented in [1], a toroidal divertorlets configuration was designed with liquid lithium as the operating liquid metal and tungsten for the slats (W–Li divertorlets). The electrical conductivity of tungsten used for simulations was 17.9 MS m^{-1} [28]. Simulations were performed with two modifications to optimize flow speeds of the system.

The first modification was the inclusion of a thin layer of electrically insulating material that coats the walls of the upward-flow channels (including slats and conductors). This allows the reduction of MHD drag, as shown in figures 13 and 14. Additionally, the coefficients $C_{M,i}$ decrease, reducing power requirements of the system.

The second modification allows the increase of the pumping force caused by the external current density $\mathbf{j}_e$. This is achieved by increasing the area of the cross section of the conductors. h_1 and h_c were changed to 1 mm and 15.3 mm, respectively (see table 1 for original magnitudes used). These two latter modifications maximize n_j and minimize C_M to ∼0.06, as assumed in [1].

Results from the latter two changes can be observed in figures 13 and 14. Figure 13 shows the the magnitudes of the MHD drag current $\sigma(\mathbf{E} + \mathbf{U} \times \mathbf{B})$ for two different configurations: (a) ∼0.07 MA m^{-2} for a W–Li insulated system and (b) ∼0.36 MA m^{-2} for the Cu–GaInSn divertorlets prototype tested. Moreover, figure 14 shows that the magnitude of C_E increased, particularly in the critical region where it significantly decreased for the case of Cu–GaInSn divertorlets (see figure 12).

A summary of results from experiments, simulations and analytical model is shown in figures 15 and 16. For generalization purposes, electric currents are shown as current densities $\mathbf{j}_0$ at the power inlet of the divertorlets system. The area used for this calculation is $A = (w_{ch} + h_s)l_s$.

The performance of divertorlets has already been observed in other liquid metal concepts [29]: an increase in magnetic field strength causes an increase in MHD drag, which could yield reducing flow speeds for the system when operating above a specific magnetic flux density. This threshold is characteristic of the liquid metal system and depends on electrical properties of the liquid metal/slats and dimensions of components.

It must be noted that the analytical model is in agreement with the performance trends of both configurations of divertorlets (Cu–GaInSn and W–Li insulated). However, there is a discrepancy between predicted values and simulation results of W–Li insulated divertorlets. The drag coefficients $(C_D)_{conds}$, $(C_D)_{branch}$ were held constant, even though the magnitude of flow speeds is different between configurations. Also, dimensions used in simulations slightly changed between configurations. A reduction of $(C_D)_{branch}$ from 1.5 to 1.25 is enough to yield agreement between the analytical model and simulation results of W–Li insulated divertorlets. This observation suffices the analysis as the search of more accurate drag coefficients is out of the scope of this work.

3.5. Heat flux exhaust

Severe temperature increases at the surface of a LM-PFC could cause intense evaporation, which in turn may result in a loss of material from the PFC into the nearby plasma [30]. Thus, the maximum permissible temperature of a liquid metal defines the critical heat flux q_{crit} that could be exhausted by a LM-PFC. The relation between these two parameters can be established through the semi-infinite slab model with a constant heat flux at the boundary [31]. This model has been used to capture the main effects of the exposure of a liquid metal flow to a heat flux from the plasma [14, 30].

Consider the direction-alternating small streams of liquid metal at the free surface of a divertorlets system (see figure 7), which move under a uniform heat flux. Assuming the thickness of the fluid flow is larger than the thermal penetration depth, then the temperature increase $\Delta T(t)$ as a function of time t at the free surface of a divertorlets system is approximated with

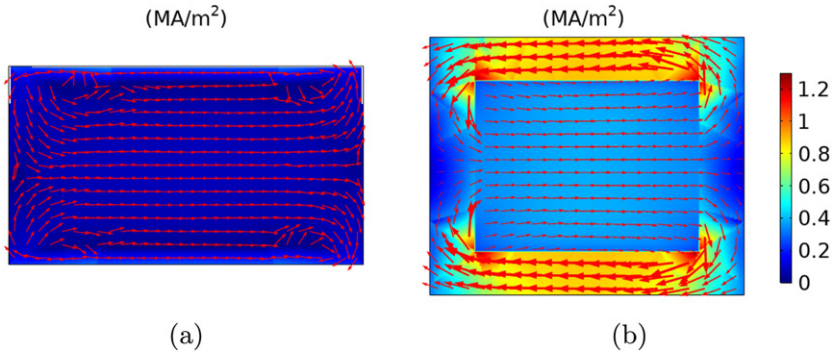

Figure 13. Toroidal–poloidal view from top of current density distribution $\sigma(\mathbf{E}+\mathbf{U}\times\mathbf{B})$ for liquid metal in a channel with conductors. Results shown are from a simulation with $I_0 = 900$ A, $|\mathbf{B}_0| = 0.3$ T. (*a*) Liquid lithium–tungsten combination with insulated walls near conductors. Plot shown does not include electric currents inside slats because of the electrical insulation around them. (*b*) Galinstan–copper combination without insulated walls near conductors. Plot shown includes currents inside liquid metal and slats.

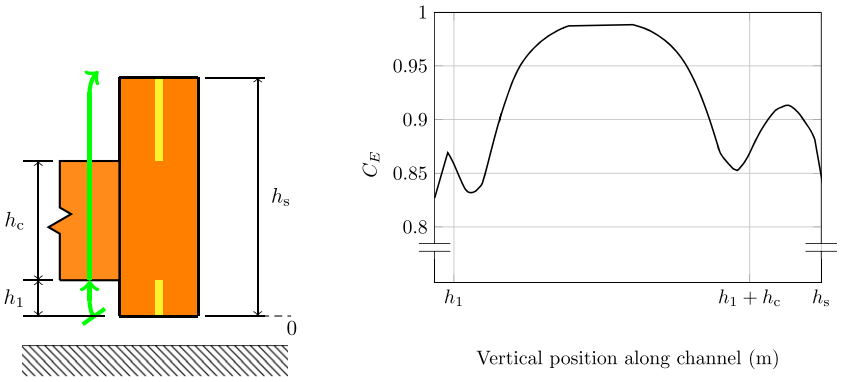

Figure 14. Ratio C_E along channel with conductors for W–Li insulated divertorlets. Plot on the right shows the values of C_E of the section highlighted in green. Results shown from simulations with $I_0 = 900$ A.

the semi-infinite slab model in equation (7) [31].

$$\Delta T(t) = 2\frac{q}{k}\sqrt{\frac{\alpha t}{\pi}}. \tag{7}$$

In equation (7), q is the incident heat flux and α and k are the thermal diffusivity and thermal conductivity of the liquid metal, respectively. The time exposure of the liquid metal to the plasma can be approximated as $t = \frac{L}{|\mathbf{U}|}$. L is the distance along which the liquid metal is exposed to the plasma (see figure 7), and $|\mathbf{U}|$ is the flow speed of the liquid metal at the free surface. After solving for the critical heat exhaust q_{crit} for a divertolets system, equation (8) is obtained:

$$q_{\text{crit}} = \frac{k\Delta T_{\text{crit}}}{2}\sqrt{\frac{\pi|\mathbf{U}|}{\alpha L}}. \tag{8}$$

For the case of liquid lithium, a maximum temperature increase ΔT_{crit} could be set at 425 K, before the growth of the evaporation rate with respect to temperature becomes exponential with increasing temperature [7]. Figure 17(*a*) shows the critical heat flux for a divertorlets system with $L = 10$ mm, which is the same magnitude chosen for the prototype tested.

The relation between q_{crit} and the distance L in equation (8) indicates there is an increasing permissible heat flux for the system with a decreasing exposure distance of the liquid metal to the plasma. For a fixed heat load of 10 MW m^{-2} [2], a divertorlets system with $L = 10$ mm requires a flow speed of $\approx$0.7 m s^{-1}, but one with $L = 1$ mm requires $\approx$0.07 m s^{-1} (see figure 17(*a*)).

Furthermore, figure 17(*b*) shows the significant change of q_{crit} for different values of L. A smaller exposure length L can either relax the requirements on flow velocity or increase the heat-exhaust capacity of the system [30]. This advantage might allow a divertorlets system to handle even more intense heat conditions as the ones estimated in [32].

Caveats about the analysis with the semi-infinite slab model have been previously mentioned [30]. Nevertheless, the semi-infinite slab model captures the main effects and allows making conclusions about the advantage of flow-path minimization (reduction of L).

Additionally, the magnitudes of L shown in figure 17(*b*) were chosen, according to the capabilities of manufacturers [33], to illustrate its relation with q_{crit}. However, a final design

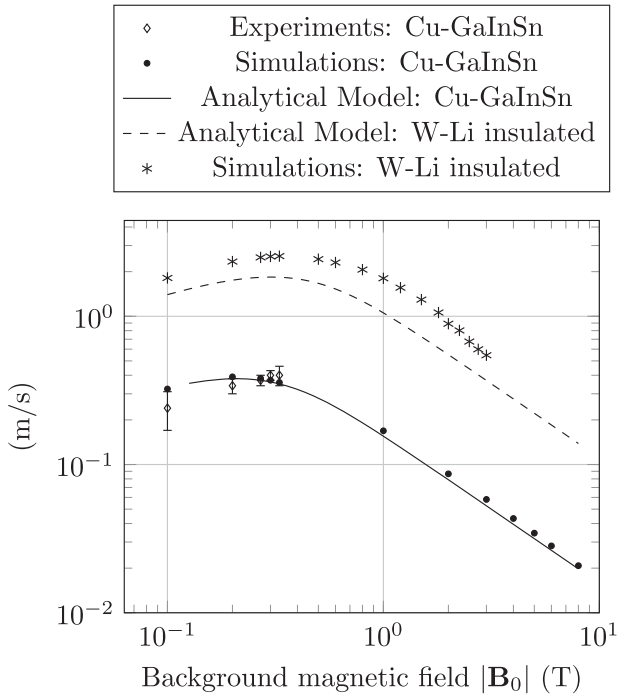

Figure 15. Average upward flow speed at $|\mathbf{j}_0| = 0.43$ MA m^{-2} ($I_0 = 900$ A).

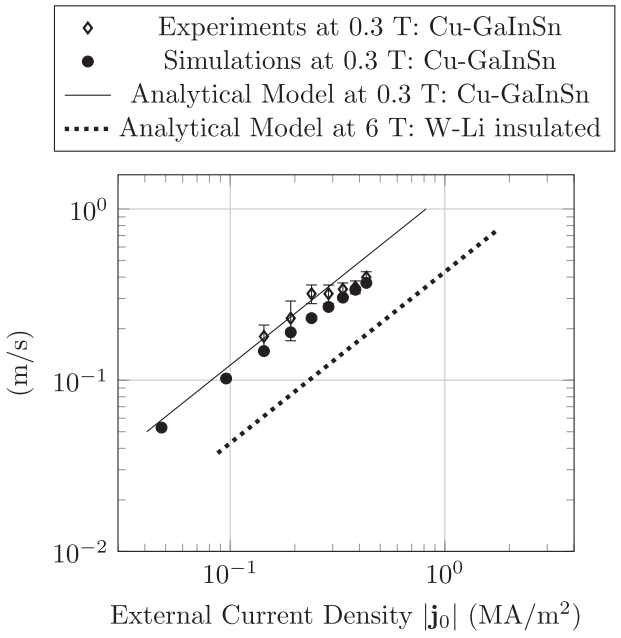

Figure 16. Average upward flow speeds on a divertorlets system at different regimes.

of a divertorlets system must allow the integration of a cooling system, and the magnitude chosen for L might impose a constraint for this purpose. Furthermore, the reduction of the distance L requires the minimization of dimensions of other components of the system, particularly the thickness w_s of the slats (see figure 4). The chosen distance L for a divertorlets configuration should be such that guarantees the structural integrity of the system against mechanical stresses during operation. The consolidation of all these aspects will be considered in future work.

A final observation is the fact that the heat flux received by a divertorlets system could generate thermally induced electric currents (thermoelectric magnetohydrodynamics (TEMHD)) [29, 34, 35]. TEMHD current densities are proportional to $S\nabla T$, where S is the Seebeck coefficient, and ∇T is the temperature gradient in the liquid metal. The temperature distribution in an operating divertorlets system depends on the cooling system integrated into it. The analysis and design of such a system have not yet been investigated.

A rough estimate of $S|\nabla T|$ can be derived as follows: the maximum temperature at the free surface of the liquid metal is assumed to be $T_2 = 580$ K, and the bottom temperature is $T_1 = 473$ K. The Seebeck coefficient at the average between these two temperatures is approximately 50.3 μV K^{-1} [36]. The temperature gradient is calculated as $|\nabla T| \approx \frac{T_2 - T_1}{w_{ch} + h_s}$. Finally, $|S\nabla T| \approx 0.21$ V m^{-1}.

From the current density range shown in figure 16, it can be concluded that $|\sigma^{-1}\mathbf{j}_0| \leqslant 0.6$ V m^{-1} for the case of liquid lithium. The latter indicates that the magnitude of $|S\nabla T|$ is comparable to $|\sigma^{-1}\mathbf{j}_0|$. However, thermally induced currents would also suffer the recycling effect due to current conservation [24], reducing the overall thermoelectric current in the liquid metal. Therefore, the overall pressure drop generated by thermoelectric currents might be still small compared to the pumping effect of the external current $\mathbf{j}_e$. Future work must include a detailed study of the localized temperature gradients and their effect in the performance of divertorlets.

3.6. Power requirements

At the reactor scale, magnetic field strengths are of the order of 3 T and higher. This condition defines a new operation regime at which viscous drag is negligible compared to MHD drag. Hence, for reactor projections, the forces that drive the flow around a slat are reduced to a balance between the pumping from the externally applied current and MHD drag, as in [1]: $\Delta P_{j\times B} \approx 0$. Thus, the electric current required for operation of a divertorlets system with $l_s = 82.3$ mm is as follows:

$$I_0 \approx \frac{|\mathbf{U}||\mathbf{B}_0|}{\eta_j(h_s + w_{ch})} \sum_{n=1}^{6} C_{M,i} C_{U,i} \Delta s_i. \tag{9}$$

Power requirements for the operation of a W–Li insulated divertorlets system at the reactor scale are shown in figure 18. Calculations shown are for a system with the dimensions of the prototype tested for this article ($L_0 = 10$ cm, see figure 7). The system was assumed to form a complete annulus at the divertor region, with a mean radius placed at a radial position $R = 5$ m from the center of a reactor.

The electrical resistance R_0 of a section of this divertorlets system with an arc length of l_s was calculated from simulations ($R_0 \approx 10.06\ \mu\Omega$). The total resistance R_T of the system is calculated as an electrical circuit in parallel $R_T = \left(\frac{2\pi R}{l_s}\right)^{-1} R_0$.

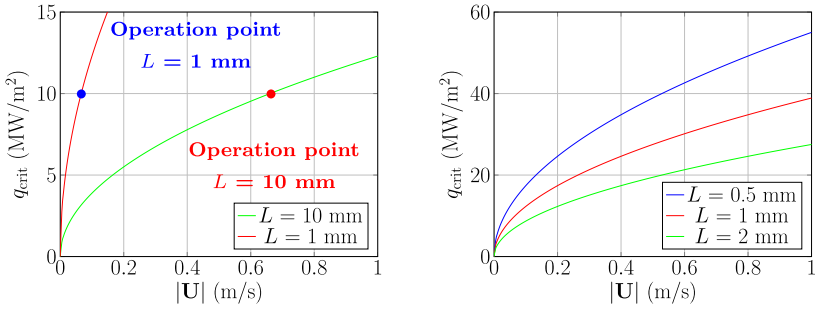

(a) Permissible heat flux for a divertorlets prototype with $L = 10$ mm

(b) Permissible heat flux at different magnitudes of L

Figure 17. Critical heat flux for a divertorlets system at different liquid metal flow speeds and $\Delta T_{crit} = 425$ K.

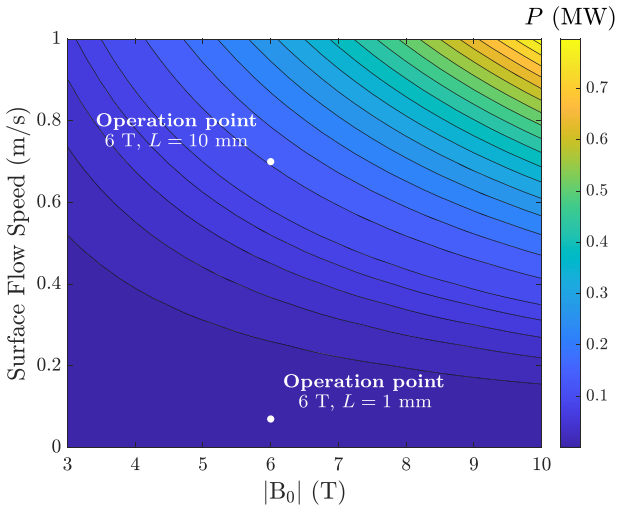

Figure 18. Reactor-scale projections for toroidal divertorlets. Note: operation points shown are for a heat load of 10 MW m^{-2}.

The total current I_T for operation is $I_T = \left(\frac{2\pi R}{l_s}\right) I_0$ (I_0 is calculated from equation (9)). Finally, the total power required for a divertorlets system is calculated as $P = I_T^2 R_T$.

As shown in figure 18, the maximum power required to operate a W–Li insulated divertorlets system is ∼0.8 MW. As a projection for reactor scale operation, this power requirement is small compared to the 300–500 MW net output expected from the DEMO power plant [37]. At a magnetic field strength of 6 T, the power requirements of the operation points shown in figure 17(*a*) are shown in figure 18.

As a note, results shown are not representative of a final design of a toroidal divertorlets system. This analysis showed a first approximation of power requirements after demonstrating the working principle of a toroidal divertorlets configuration. The inclusion of a cooling system and instabilities from rapid heating on the liquid metal must be regarded. The integration of all these aspects will be considered in future work.

4. Conclusions

This work presents the analysis of the performance of a toroidal divertorlets configuration at low magnetic field intensities ($|\mathbf{j}_e \times \mathbf{B}_0| \leqslant 0.23$ MN m^{-3}). Experiments demonstrated the cyclical flow of liquid metal around the slats of a toroidal divertorlets configuration, and simulations showed agreement with experimental measurements. Based on this, an analytical model to describe flow speeds on a toroidal divertorlets device was derived and compared with simulation results.

Agreement between simulations and analytical model was shown. While there is a discrepancy in the flow speed trends between experimental results and simulations/analytical model, the error could be attributed to liquid-metal oxidation, corrosion of the faces of the slats and pressure drops generated by the plastic tubes used for measurements.

Furthermore, projections for the performance of this device at the reactor scale were extrapolated using the model derived. Results from projections indicate that the toroidal divertorlets meets the criteria stated in previous work [1] for qualities desired in a non-evaporative liquid metal solution for heat removal. Moreover, it was shown that the minimization of the flow path length could allow a divertorlets system to withstand heat loads of 10 MW m^{-2} and above, while operating in a flow speed range that reduces MHD drag.

Future upgrades for a toroidal divertorlets configuration must include the analysis of thermoelectric magnetohydrodynamics effects on the system and the integration of a cooling system, while looking forward to achieving flow path length minimization and maintaining structural integrity.

Acknowledgments

This work was supported by the United States Department of Energy through Field Work Proposal No. 1019, Domestic Liquid Metal Plasma Facing Component Development. The research described in this paper was conducted under the Laboratory Directed Research and Development (LDRD) Program

at Princeton Plasma Physics Laboratory, a national laboratory operated by Princeton University for the US Department of Energy under Prime Contract No. DE-AC02-09CH11466. This manuscript is based upon work supported by the US Department of Energy, Office of Science, Office of Fusion Energy Sciences.

ORCID iDs

F. Saenz https://orcid.org/0000-0001-7456-590X
Z. Sun https://orcid.org/0000-0002-7224-3592
A.E. Fisher https://orcid.org/0000-0003-1744-6984
B. Wynne https://orcid.org/0000-0002-0593-2195
E. Kolemen https://orcid.org/0000-0003-4212-3247

References

[1] Fisher A.E., Sun Z. and Kolemen E. 2020 Liquid metal divertorlets concept for fusion reactors *Nucl. Mater. Energy* **25** 100855
[2] Loarte A. *et al* 2007 Progress in the ITER Physics Basis Chapter 4: power and particle control *Nucl. Fusion* **47** S203–63
[3] Majeski R. *et al* 2013 Particle control and plasma performance in the lithium tokamak experiment *Phys. Plasmas* **20** 056103
[4] Evtikhin V.A. *et al* 2002 Lithium divertor concept and results of supporting experiments *Plasma Phys. Control. Fusion* **44** 955–77
[5] Kaita R. *et al* 2007 Low recycling and high power density handling physics in the current drive experiment-upgrade with lithium plasma-facing components *Phys. Plasmas* **14** 056111
[6] Yang Q. *et al* 2017 Development of the flowing liquid lithium limiter for east tokamak *Fusion Eng. Des.* **124** 179–82 Proc. 29th Symp. Fusion Technology (SOFT-29) Prague, Czech Republic, 5–9 September 2016
[7] de Castro A., Moynihan C., Stemmley S., Szott M. and Ruzic D.N. 2021 Lithium, a path to make fusion energy affordable *Phys. Plasmas* **28** 050901
[8] Sun Z., Hu J., Zuo G., Ren J., Li J., Zakharov L. and Mansfield D. 2013 Development of and experiments with liquid lithium limiters on ht-7 *J. Nucl. Mater.* **438** S899–904 Proc. 20th Int. Conf. Plasma–Surface Interactions in Controlled Fusion Devices
[9] Kaita R. 2019 Fusion applications for lithium: wall conditioning in magnetic confinement devices *Plasma Phys. Control. Fusion* **61** 113001
[10] Mansfield D.K. *et al* 1996 Enhancement of tokamak fusion test reactor performance by lithium conditioning *Phys. Plasmas* **3** 1892–7
[11] Zakharov L.E. 2019 On a burning plasma low recycling regime with P DT = 23–26 MW, Q DT = 5–7 in a JET-like tokamak *Nucl. Fusion* **59** 096008
[12] Kolemen E., Hvasta M., Majeski R., Maingi R., Brooks A. and Kozub T. 2019 Design of the flowing liquid torus (flit) *Nucl. Mater. Energy* **19** 524–30
[13] Ruzic D.N., Xu W., Andruczyk D. and Jaworski M.A. 2011 Lithium-metal infused trenches (LiMIT) for heat removal in fusion devices *Nucl. Fusion* **51** 102002
[14] Shimada M. and Hirooka Y. 2014 Actively convected liquid metal divertor *Nucl. Fusion* **54** 122002
[15] Morley N.B. and Burris J. 2003 The MTOR LM-MHD flow facility, and preliminary experimental investigation of thin layer, liquid metal flow in a 1/r toroidal magnetic field *Fusion Sci. Technol.* **44** 74–8
[16] Liu J. and Yi L. 2018 *Liquid Metal Biomaterials: Principles and Applications* (*Springer Series in Biomaterials Science and Engineering*) (Berlin: Springer)
[17] Davison H.W. 1968 *Compilation of Thermophysical Properties of Liquid Lithium NASA-TN-D-4650* National Aeronautics and Space Administration
[18] Fisher A.E., Kolemen E. and Hvasta M.G. 2018 Experimental demonstration of hydraulic jump control in liquid metal channel flow using Lorentz force *Phys. Fluids* **30** 067104
[19] COMSOL 2020 COMSOL Multiphysics Reference Manual (https://doc.comsol.com/5.6/doc/com.comsol.help.comsol/COMSOL_ReferenceManual.pdf)
[20] COMSOL 2020 CFD Module User's Guide (https://doc.comsol.com/5.6/doc/com.comsol.help.cfd/CFDModuleUsersGuide.pdf)
[21] COMSOL 2020 AC/DC Module User's Guide (https://doc.comsol.com/5.6/doc/com.comsol.help.acdc/ACDCModuleUsersGuide.pdf)
[22] Afifeh M., Hosseinipour S.J. and Jamaati R. 2019 Nanostructured copper matrix composite with extraordinary strength and high electrical conductivity produced by asymmetric cryorolling *Mater. Sci. Eng.* A **763** 138146
[23] Cui Y., Ding Y., Xu S., Yang Z., Zhang P., Rao W. and Liu J. 2018 Liquid metal corrosion effects on conventional metallic alloys exposed to eutectic gallium–indium alloy under various temperature states *Int. J. Thermophys.* **39** 1–14
[24] Davidson P.A. 2001 *An Introduction to Magnetohydrodynamics* (*Cambridge Texts in Applied Mathematics*) (Cambridge: Cambridge University Press)
[25] Miyazaki K., Inoue S., Yamaoka N., Horiba T. and Yokomizo K. 1986 Magneto-hydro-dynamic pressure drop of lithium flow in rectangular ducts *Fusion Technol.* **10** 830–6
[26] Heddleson C.F., Brown D.L. and Cliffe R.T. 1957 Summary of drag coefficients of various shaped cylinders *Technical Report* Defense Technical Information Center Fort Belvoir, VA
[27] Mynard J.P. and Valen-Sendstad K. 2015 A unified method for estimating pressure losses at vascular junctions: pressure losses at vascular junctions *Int. J. Numer. Methods Biomed. Eng.* **31**
[28] Hust J.G. and Lankford A.B. 1984 Thermal conductivity of aluminum, copper, iron, and tungsten for temperatures from 1 K to the melting point *Technical Report* (US Department of Energy Office of Scientific and Technical Information)
[29] Xu W., Curreli D. and Ruzic D.N. 2014 Computational studies of thermoelectric MHD driven liquid lithium flow in metal trenches *Fusion Eng. Des.* **89** 2868–74
[30] Jaworski M.A., Brooks A., Kaita R., Lopes-Cardozo N., Menard J., Ono M., Rindt P. and Tresemer K. 2016 Upgrades toward high-heat flux, liquid lithium plasma-facing components in the NSTX-U *Fusion Eng. Des.* **112** 93–101
[31] Incropera F. 2006 *Fundamentals of Heat and Mass Transfer* 6th edn (New York: Wiley)
[32] Eich T. *et al* 2013 Scaling of the tokamak near the scrape-off layer H-mode power width and implications for ITER *Nucl. Fusion* **53** 093031
[33] DUNLEE Dunlee's co-development of 3D-printed tungsten parts helps customers succeed 122022 Document No. 452299155001 (https://dunlee.com/c-dam/dunlee/downloads/5219172_Adaption_Dunlee_WhitePaper_Tungsten.pdf) (accessed 1 2 2022)
[34] Shercliff J.A. 1979 Thermoelectric magnetohydrodynamics *J. Fluid Mech.* **91** 231–51
[35] Jaworski M.A., Gray T.K., Antonelli M., Kim J.J., Lau C.Y., Lee M.B., Neumann M.J., Xu W. and Ruzic D.N. 2010 Thermoelectric magnetohydrodynamic stirring of liquid metals *Phys. Rev. Lett.* **104** 094503
[36] Fiflis P., Kirsch L., Andruczyk D., Curreli D. and Ruzic D.N. 2013 Seebeck coefficient measurements on Li, Sn, Ta, Mo, and W *J. Nucl. Mater.* **438** 224–7
[37] EUROFusion The demonstration power plant: DEMO (https://euro-fusion.org/programme/demo/) (accessed 5 April 2022)